

On the origin of non self-gravitating filaments in the ISM

Patrick Hennebelle^{1,2}

¹ Laboratoire AIM, Paris-Saclay, CEA/IRFU/Sap - CNRS - Université Paris Diderot, 91191, Gif-sur-Yvette Cedex, France

² LERMA (UMR CNRS 8112), Ecole Normale Supérieure, 75231 Paris Cedex, France

Preprint online version: August 3, 2018

ABSTRACT

Context. Filaments are ubiquitous in the interstellar medium as recently emphasized by Herschel, yet their physical origin remains elusive

Aims. It is therefore important to understand the physics of molecular clouds to investigate how filaments form and what is the role played by various processes such as turbulence and magnetic field.

Methods. We use ideal MHD simulations to study the formation of clumps in various conditions including different magnetization and Mach numbers as well as two completely different setup. We then perform several analysis to compute the shape of the clumps and their link to velocities and forces using various approaches.

Results. We find that on average, clumps in MHD simulations are more filamentary than clumps in hydrodynamical simulations. Detailed analyses reveal that the filaments are in general preferentially aligned with the strain which means that these structures simply result from the stretch induced by turbulence. Moreover filaments tend to be confined by the Lorentz force which therefore lead them to survive longer in magnetized flows. We show that they have in all simulations a typical thickness equal to a few grid cells suggesting that they are primarily associated to the energy dissipation within the flow. We estimate the order of magnitude of the dissipation length associated to the ion-neutral friction and conclude that in well UV shielded regions it is of the order of 0.1 pc and therefore could possibly set the typical size of non self-gravitating filaments.

Conclusions. Filaments are ubiquitous because they are the results of the very generic turbulent strain and because magnetic field help to keep them coherent. We suggest that energy dissipation is playing a determinant role in their formation.

Key words. Turbulence - Stars: formation - Interstellar medium:structure - Magnetic field

1. Introduction

For more than three decades, the evidences for the filamentary structure of the molecular clouds seen through their CO emission has become clear (e.g. Ungerechts & Thaddeus 1987, Bally et al. 1987). The far-IR all-sky IRAS survey (Low et al. 1984) also revealed the ubiquitous filamentary structure of the ISM, and discovered the cirrus clouds, i.e. the filamentary structure of the diffuse interstellar medium (ISM).

Thanks to its unprecedented sensitivity and large-scale mapping capabilities, Herschel has now provided a unique view of these filamentary structures of cold dust (e.g. Miville-Deschênes et al. 2010, Ward-Thompson et al. 2010, André et al. 2010). One of the main and intriguing findings is the very large range of column densities – a factor of 100 between the most tenuous ($N_{H_2} = 2 \times 10^{20} \text{ cm}^{-2}$) and most opaque ($N_{H_2} \sim 10^{23} \text{ cm}^{-2}$) of the observed filaments in several fields contrasting with a narrow range of filament thickness (between 0.03 and 0.2 pc) barely increasing with the central column density (Arzoumanian et al. 2011). The present study is largely motivated by this result though as described below is too premature to directly address it.

While the filamentary nature of molecular cloud is probably linked to their turbulence, the exact mechanism by which this happens remains to be understood. In many pub-

lished numerical simulations, filaments are clearly present (e.g. de Avillez & Breitschwerdt 2005, Heitsch et al. 2005, Joung & MacLow 2006, Padoan et al. 2007, Hennebelle et al. 2008, Price & Bate 2008, Banerjee et al. 2009, Inoue et al. 2009, Nakamura & Li 2008, Seifreid et al. 2011, Vázquez-Semadeni et al. 2011, Federrath & Klessen 2013) but again the exact reason of their formation mechanism is not very clearly analyzed. Based on the evidence for higher velocities in the outer part of the filaments, Padoan et al. (2001) proposed that they form through the collision of two shocked sheets. Another type of explanation invokes instabilities in self-gravitating sheets (e.g. Nagai et al. 1998). Although it is clear that since filaments are denser than their environment some compression must necessarily occurs, it is important to understand in greater details the conditions in which the filament formation happens. In particular an important question is the origin of the elongation. Is the elongation produced by the contraction along two directions like what would happen in a shock or in a converging flow? Or is the elongation the result of the stretching of the fluid particles along one direction? The purpose of this paper is to investigate these questions.

The paper is organized as follows. In the second part we describe the analysis that will be performed to the clumps and the filaments formed in the numerical simulations. We also describe the various runs that we carry out to under-

stand the filament origin. In the third section, we present a simple but enlightening preliminary numerical experiment that clearly demonstrates that the mechanism we propose can actually work. In the fourth section we show the numerical simulations and present the clump statistics such as their aspect ratio, length and thickness distributions. In the fifth section we analyze the link between the filament orientation, the velocity field and the forces. The sixth section provides further discussion regarding the filament thickness as well as simple orders of magnitude which suggest that ion-neutral friction could possibly explain their thickness. The seventh section concludes the paper.

2. General analysis and Numerical simulations

2.1. Structure analysis

In the present paper we perform numerical simulations relevant for the diffuse and moderately dense ISM. The mean density we consider goes from 5 cm^{-3} to about 100 cm^{-3} while the largest densities is larger than a few 10^3 cm^{-3} .

2.1.1. Definitions

The first difficulty when discussing clouds is actually to define them. To identify structures in this work, we follow a simple approach. The first step is to choose a density threshold (two of them will be used through the paper namely $n_{thres} = 50$ and 200 cm^{-3}) and to clip the density field. Then using a friend of friend analysis, the connected cells are associated to form a clump. Once this is done, the structure properties can easily be computed. The structures obtained through this process are called clumps. In many occasions we will also refer to filaments. Filaments as clumps are not well identified objects and although it could be easy to adopt an arbitrary criterion like an aspect ratio above some values, that would not bring much information. When we use the word *filament* it will simply refer to a clump that is sufficiently elongated say by a factor of about 5 or more.

2.1.2. Inertia Matrix

To estimate the shape of a structure, it is convenient to compute the Inertia Matrix and its eigenvalues and eigenvectors. The inertia matrix is a three by three matrix defined as: $I_{ij} = \int x_i x_j dm$ where x_i are the coordinates of the cells belonging to the structure associated to its center of mass. The three eigenvectors give the three main axis of the structure which correspond to symmetry axis if the structure admits some while the eigenvalues represent the moment of inertia of the structure with respect to the three eigenvectors. From the inertia momentum, I_i , we can get an estimate of the structure size $\mu_i = \sqrt{I_i/M}$ where M is the structure mass. In the case of filaments for example, the eigenvector associated with the largest eigenvalue tends to be aligned with the main axis of the filament while the two other eigenvectors tend to be perpendicular to the filament axis. In the following, we will refer to the eigenvector associated to the largest eigenvalue as the main axis. We will also quantify the aspect ratio of structures by computing the ratio of eigenvalues. We will in particular consider μ_1/μ_3 and μ_2/μ_3 , the ratios of the smallest over largest structure size and the intermediate over largest respectively.

Note that one of the difficulties with this approach is that a thin but curved filaments will have moments of inertia that reflect the curvature rather than the effective thickness. For this reason, we will use in the paper a second method to characterize their shape.

2.2. Strain tensor

The strain tensor is another useful quantity that we will use to perform our analysis. It is obtained by considering the velocity difference between two fluid particles located in \mathbf{r} and $\mathbf{r} + d\mathbf{r}$. One gets $v_i(\mathbf{r} + d\mathbf{r}) - v_i(\mathbf{r}) = \partial_j v_i d\mathbf{r}_j$ where summation over repeating indices is used. The three by three matrix, $\partial_j v_i$, can be splitted in its anti-symmetric part $A_{i,j} = (\partial_j v_i - \partial_i v_j)/2$, which describes the rotation of the fluid element and its symmetric part $S_{i,j} = (\partial_j v_i + \partial_i v_j)/2$, which describes the shape modification of the fluid element and is called the infinitesimal strain tensor. The trace $S_{i,i}$, which is equal to the divergence of \mathbf{v} , describes the change of volume. The symmetric part can be diagonalised leading to three eigenvalues, s_i , where we assume that $s_3 > s_2 > s_1$. The eigenvector associated to the largest eigenvalue, s_3 , describes the axis along which the fluid particle is mostly elongated, below we call it the strain. Note that in principle since the divergence of the fluid is non zero, all eigenvalues could be negative which would then correspond to a global contraction. In practice, in our simulations this is almost never the case at the scale of the clumps. The two other eigenvectors associated to the two other eigenvalues correspond to the directions along which the shape of the fluid particle is either stretched or compressed depending on their signs.

Note that computing the strain tensor is not straightforward since it requires to take the velocity gradients between cells. Moreover, because of the numerical diffusion, the gradients at the scale of the mesh are artificially smoothed. To limit this problem, we smooth the simulation by a factor three computing the mean density weighted velocity within the smoothed cells. Then we compute all velocity gradients using simple finite differences and we compute the mean gradients by summing over all cells which belong to the structure. Finally, we use these values to compute S_{ij} .

2.2.1. A simple skeleton-like approach

Another useful approach is to determine an average line characteristic of the clump shape. Such algorithm has been developed in the context of Cosmology to reconstruct the filaments leading to the so-called skeleton (Sousbie et al. 2009). Here we follow a simpler approach which is well suited for our analysis. The first step is to select the direction (x , y or z) along which the structure is the longest. Then, we can subdivide it into a number of slice, n_{sl} , of a given length in the selected direction. Each slice, i , can itself be divided into n_{sr} connect regions, that is to say regions in which all cells are connected to each other through their neighbours. Each of these sub-regions, j , belongs to a different branch within the structure. Then the center of mass, G_i^j of each of these sub-regions within each slice, can be computed leading to an ensemble of points G_i^j . For each of them we look for the nearest neighbour, G_i^j of G_i^j belonging to the slices $i-1$ or $i+1$. Finally, we calculate the vector $\mathbf{u}_i^j = \pm \mathbf{G}_i^j G_i^j / G_i^j G_i^j$ which gives the local direction of

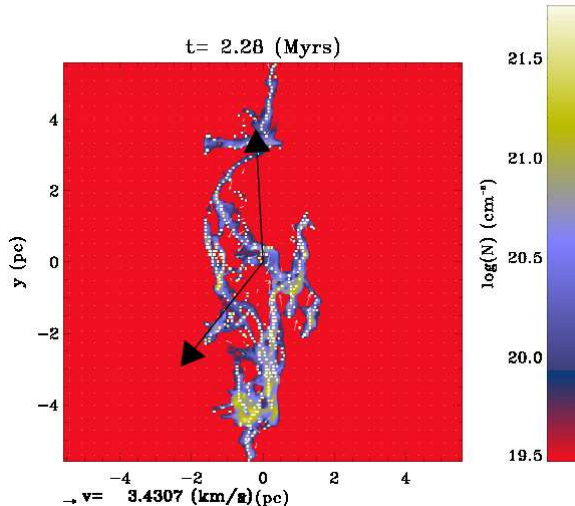


Fig. 1. Column density and velocity field for one of the clumps formed in the MHD simulations. The white points represent the local mass center G_{ij} and constitute the skeleton of the clump. The upwarding arrow represents the filament main axis as computed with the inertia matrix. The downwarding arrow represents the main direction of the strain as computed with the strain tensor.

the branch to which G_i^j belongs. The sign is then chosen in order to insure $\mathbf{u}_i^j \cdot \mathbf{X} > 0$ where X represents the selected axis, x , y or z . Connecting all G_i^j to their respective neighbours, we obtain a curve that represents the mean local direction. Figure 1 shows an example of a clump extracted from the fiducial MHD simulation presented below. The white cells represent the position of the G_i^j , as can be seen they follow well each branch of the clump. The two arrows represent the clump main axis (computed with the inertia matrix as explained above) and the strain (computed with the strain tensor). Note that the clump is quite filamentary and that the main axis represented by the vertical arrow follows well the filament direction.

Once the \mathbf{u}_i^j are known, it is an easy task to estimate the distance, r_M , from a given filament cell to the skeleton. Since any cell belonging to the structure, is associated to a sub-region, one can calculate $r_M = |\mathbf{G}_i^j \mathbf{M} \times \mathbf{u}_i^j|$, where M is the cell center. In the paper, we make use of the vectors \mathbf{u}_i^j to compute various quantities as the mean component of various forces. The mean radius is then defined as $r_c = \Sigma r_M dm / \Sigma dm$ where dm is the mass within the cell and where the sum is taken over all clump cells. We stress that the thickness, r_c calculated by this definition is really measuring the thickness of the clump substructures and not the mean size of the clumps which would take into account the distance between the various branches. This is particularly clear in Fig. 1 where the distance between the branches is of the order of a few pc while in most regions of the clump, the size of the individual branches is typically ten times smaller.

2.3. Description of numerical simulations

2.3.1. Code and resolution

We use the Ramses code (Teyssier 2002, Fromang et al. 2006) to perform the simulations. Ramses uses adaptive mesh refinement and solve the ideal MHD equations using the Riemann HLLD solver (Miyoshi & Kuzano 2005). It uses constraint transport method to ensure that $\text{div} \mathbf{B}$ is maintained to zero. The cooling corresponds to the standard ISM cooling (e.g. Wolfire et al. 1995) as described in Audit & Hennebelle (2005) and includes Lyman α , C^+ and O lines. The heating is due to the photo-electric effect on small dust grains. Here we carry simulations which have a based grid of 512^3 cells. Then depending on the simulations we either add another or two other AMR levels leading to an effective resolution in the most refined areas of 1024^3 to 2048^3 cells. The refinement criteria is based on density. Any cell which has a density larger than 50 cm^{-3} is refined to resolution 1024^3 and when it is allowed, cells denser than 200^{-3} are refined to resolution 2048^3 . The high resolution run allows us to check for numerical convergence and to verify by comparison with the coarser runs that the AMR does not introduce any major bias.

2.3.2. Initial conditions

Our initial conditions for the fiducial simulations consist in a uniform medium in density, temperature and magnetic field on which a turbulent velocity field has been superimposed. The latter is generated using random phases and presents a powerspectrum of $k^{-5/3}$. No forcing is applied and the turbulence is therefore decaying. The initial density is equal to 5 cm^{-3} and the initial temperature $T = 1600 \text{ K}$ leading to a pressure of 8000 K cm^{-3} typical of the ISM. The magnetic field is initially aligned along the x-axis and has an intensity of about $5 \mu\text{G}$ (or 0 in the hydrodynamical case). The initial rms velocity is equal to 10 km s^{-1} . Since these simulations have no energy injection, the turbulence is decaying in a few crossing times which is thus an important quantity to estimate. It is however not straightforward since it is evolving with time. The total velocity to be considered is the sum of the rms velocity and the wave velocity (sound and Alfvén waves). Initially both are of the order of 3-4 km s^{-1} but they raise to about 10 km s^{-1} in the diffuse gas when the gas breaks up into warm and cold phase leading to a total velocity of the order of 20 km s^{-1} . Thus we estimate the crossing time to be of the order of 2-3 Myr. It is worth stressing that the crossing time at the scale of the clumps is obviously much shorter thus it is probably the case that their properties are setup much quicker than a box crossing time.

We have performed several runs. The run that we consider as being fiducial has an effective resolution of 1024^3 cells and is magnetized. The initial velocity dispersion is 10 km s^{-1} which corresponds to a typical Mach number with respect to the cold gas of about $\mathcal{M} = 10$ since its sound speed is about 1 km s^{-1} . To investigate the effect that the magnetic field has on the medium structure, we have performed an hydrodynamical run at the same resolution. Next we have explored the influence of the Mach number \mathcal{M} by dividing the initial velocity amplitude by 3 and then by 10. We refer to these two runs as Mach $\mathcal{M} = 3$ and 1 respectively keeping in mind that this corresponds

to the initial rms velocity. Then to investigate the influence of the resolution, we have repeated the fiducial run (magnetized and $\mathcal{M} = 10$) with an effective resolution of 2048^3 cells. Note that in order to compare well this simulation with the fiducial run, we have identified the clumps at the *same* resolution which means that cells having an effective resolution of 2048^3 have been smoothed before performing the analysis. Below the results are given for these 5 simulations. To show that they do not strongly depend on time evolution, we also present all statistics at two different timesteps of the hydrodynamical run, one after about 1/2-1 crossing times and one at about 1.5-2. In order to verify that no spurious effect has been introduced by the magnetic field being initially aligned with the mesh, we have repeated the simulation with $5 \mu\text{G}$ and $\mathcal{M} = 10$ but tilting the initial magnetic field with respect to the mesh from 45° . The corresponding result is shown in appendix A, no significant difference with the aligned case is seen.

Finally, in order to verify the robustness of our results, we have also used another very different type of setup, namely converging flow type simulations which include self-gravity. These simulations are very similar to the ones presented in Hennebelle et al. (2008) and in Klessen & Hennebelle (2010). They consist in imposing from the x-boundaries two streams of warm neutral medium having velocities of about $\pm 20 \text{ km/s}$, density of 1 cm^{-3} and temperature of 8000 K . The magnetic field is initially uniform and oriented along the x-axis. Unlike the decaying simulations, no velocity field is initially imposed in the computational box. Moreover the turbulence which develops is sustained by the energy due to the incoming flow. Also the mean density is typically ten times higher in the colliding flow simulations. Four simulations of this type have been performed. Three simulations have an effective resolution of 1024^3 cells amongst which one is hydrodynamical, one has an initial magnetic field of $2.5 \mu\text{G}$ and one has $5 \mu\text{G}$. The fourth one is identical to the intermediate resolution simulation with $2.5 \mu\text{G}$ but has an effective resolution of 4096^3 cells. In spite of these important differences between the decaying and colliding simulations, the conclusions we inferred remain unchanged. All the trends which are inferred in the decaying runs are recovered in the colliding flow runs. Therefore, for the sake of conciseness we present the corresponding results in the appendix B.

3. A simple preliminary numerical experiment

Before proceeding to the complex turbulent simulations, we present two simple numerical simulations that illustrate some of the conclusions that will be drawn later. It consists in a spherical cloud which has a strong shear initially and therefore is prone to form a filament. More precisely, the spherical cloud of density 100 cm^{-3} , temperature 100 K and radius 0.5 pc is placed in the middle of the computational box and is embedded into a diffuse and warm medium of density 1 cm^{-3} and temperature 8000 K . The total box size is 20 pc . A transverse velocity gradient along the x-axis of $1.5 \text{ km s}^{-1} \text{ pc}^{-1}$ is initially imprinted through the box. Finally, a turbulent velocity field having a total rms dispersion of 5 km s^{-1} is super-imposed in the box. The reason of superimposing such velocity field is to create self-consistently perturbations that disturb the forming filament. Two such simulations have been performed, the first one is purely hydrodynamical while the second one

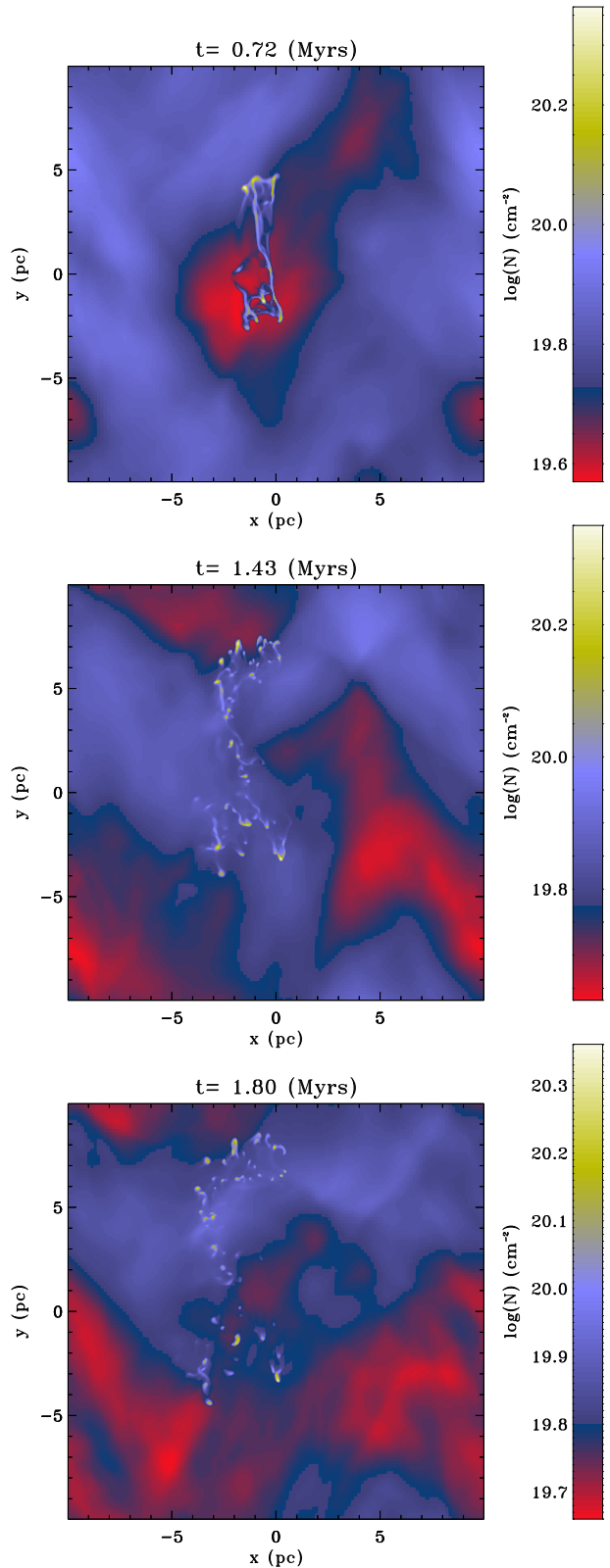


Fig. 2. Formation of a filament from a spherical cloud in the presence of shear, $v_y(x)$. The column density for three snapshots is displayed. Hydrodynamical case. The filament quickly fragments in many cloudlets.

has a magnetic field of $1 \mu\text{G}$, uniform initially and oriented along the x-axis therefore perpendicular to the initial main component of the velocity field.

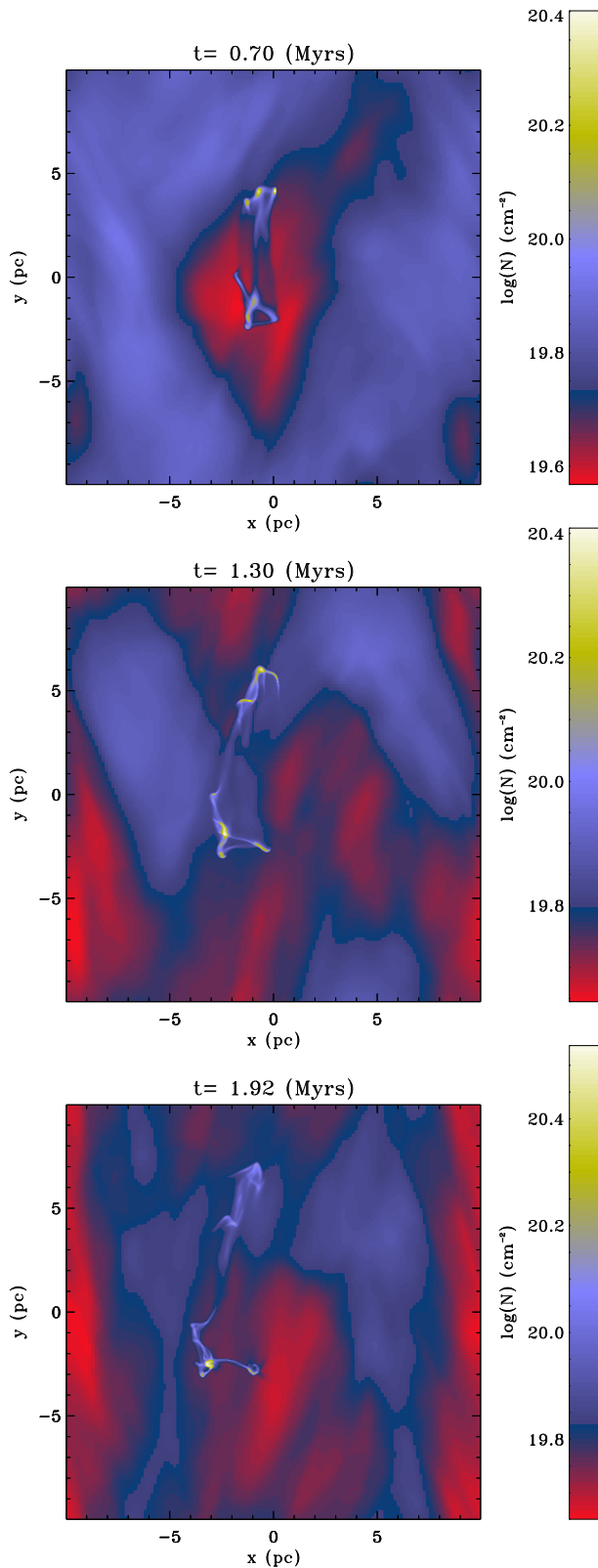


Fig. 3. Same as Fig. 2 in the MHD case. A weak magnetic field ($1 \mu G$) along the x-axis is permeating the cloud initially. The filament remains much more coherent than in the hydrodynamical case.

Figure 2 shows the column density for three snapshots of the hydrodynamical simulation. As it is clear from the figure, the initially spherical cloud is stretched and evolves

in a filament because of the shear. In the same time the non-linear fluctuations induced by the surrounding medium perturb the cloud and likely trigger the growth of various instabilities (like Kelvin-Helmholtz). The complex pattern displayed in the three snapshots is the result of the uniform shear and the turbulent fluctuations present in the surrounding medium. After 1.6 Myr the third panel shows that the filament is totally destroyed and broken in many cloudlets.

Figure 3 shows the magnetized run. The early evolution of the dense cloud is similar initially. Due to the initial shear, a filament forms. However, the late evolution is quite different. The filament although subject to large fluctuations induced by the surrounding turbulent medium, remains much more coherent. This is because since the cloud is threatened by a magnetic field initially, the pieces of fluid are connected to each others through the field lines. Moreover, the shear that tends to form the filament, amplifies the magnetic field making its influence stronger. Indeed, as the filament is getting stretched, the magnetic field is amplified along the y-axis and becomes largely parallel to the filament at the end of the simulation. This behaviour is qualitatively in good agreement with the studies of the development of the Kelvin-Helmholz instability which have been performed by various teams (e.g. Frank et al. 1996, Ryu et al. 2000). In these studies it is found that even weak magnetic field significantly modify the evolution of flow making it much less unstable. Stronger fields, on the other hand, can completely stabilize the flow against this instability.

This simple experiment suggests a scenario for the formation of filaments. The gas is compressed by converging motions but in the same time, the fluid particle possesses solenoidal modes inherited from the turbulent environment that tends to stretch it. In the absence of magnetic field, the pieces of fluid can easily move away from each other. When a magnetic field is present, there are more tight to each other and the filament remains coherent for longer times.

4. Clump geometry

4.1. Qualitative description of decaying turbulence simulations

Figures 4 and 5 show one snapshot at roughly one crossing time in the hydrodynamical and MHD cases. Column density (top panels) and density together with velocity fields are shown (bottom panels). The Column density is obtained by simple integration through the box and the density corresponds to the value in the $z = 0$ plane. As expected in both cases due to the large rms Mach numbers (about 3 initially to 1 in the WNM and 10 in the CNM), large density contrast develop partly because of the 2-phase structure and partly because of the supersonic motions. The hydrodynamical and MHD cases present however obvious differences. Overall the hydrodynamical case appears to be less filamentary than the MHD case in which very high aspect ratio structures can be seen both in the column density and in the density. Some filamentary structures are also visible in the hydrodynamical case but they have smaller aspect ratios. Moreover as seen from the density and velocity fields, it is often the case that the velocity field is perpendicular to the elongated structure suggesting that shocks are trig-

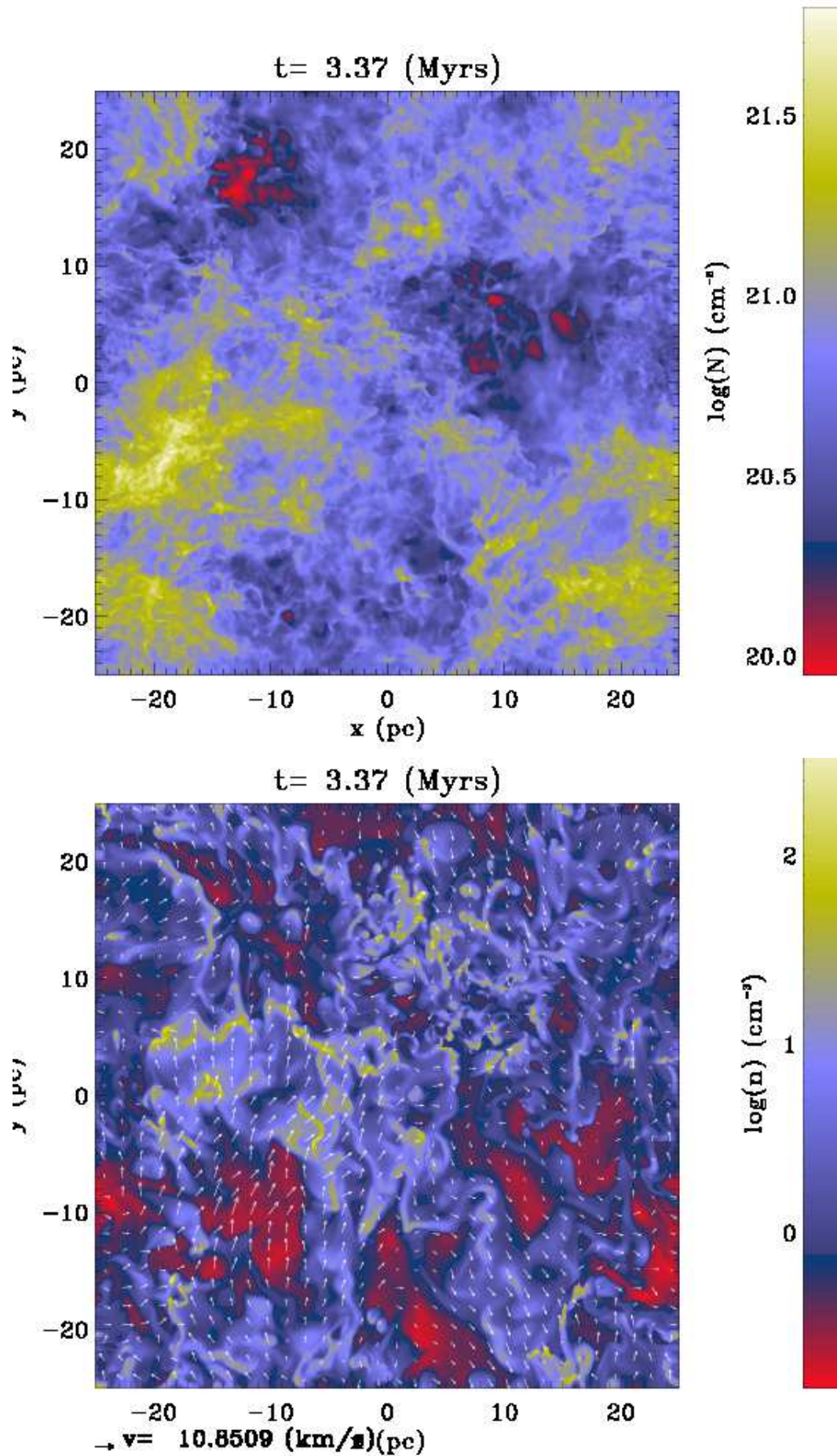


Fig. 4. Column density, density and velocity fields for one snapshot of the decaying turbulence experiment in the hydrodynamical case.

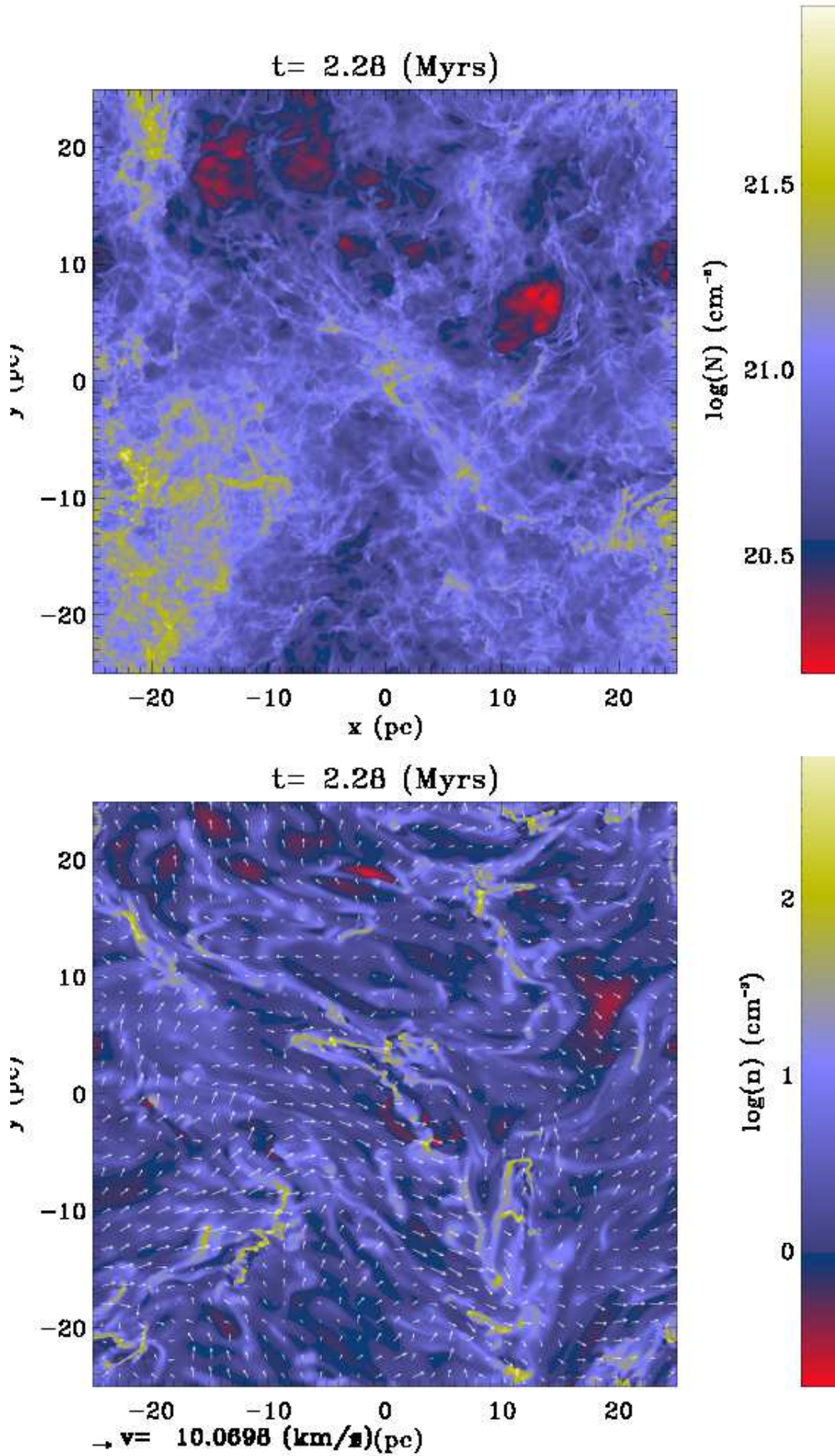


Fig. 5. Column density, density and velocity fields for one snapshot of the decaying turbulence experiment in the MHD case.

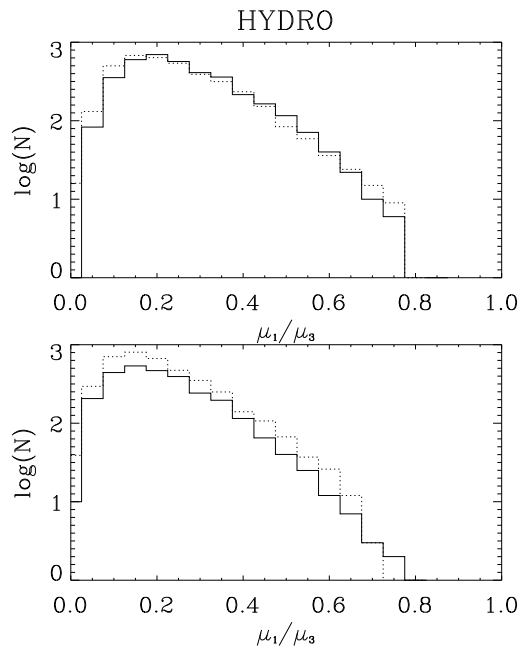


Fig. 6. Distribution of aspect ratio, μ_3/μ_1 of the clumps (threshold 50 cm^{-3} : upper panel and 200 cm^{-3} : lower panel) in the hydrodynamical simulation at time $t = 1.52$ Myr (dotted lines) and $t = 3.37$ Myr (solid lines).

gering them. Indeed these structures are mainly sheets as will be shown later.

To be complete, it should be said that at the beginning of our calculations which we recall start with uniform density and a velocity field constructed with random phases, more high aspect ratio structures form in the hydrodynamical phase. However, this is a transient phenomenon due to our somehow arbitrary initial conditions. These filaments quickly reexpand leading to the type of morphology seen in Fig. 4. It is worth stressing that this visual impression of the MHD simulations being more filamentary is clearly visible in various other works (Padoan et al. 2007, Hennebelle et al. 2008, Federrath & Klessen 2013).

Beyond this visual impression, it is important to carefully quantify the aspect ratio which is the purpose of the following section.

4.2. Axis ratio of clumps

Here we attempt to quantify the clump aspect ratio using two different methods namely the inertia matrix and the skeleton approach.

4.2.1. Aspect ratio from inertia matrix

As explained in Section 2.1.2, the inertia matrix is computed for all clumps and the aspect ratio is estimated as the quantity $\sqrt{I_1/I_3} = \mu_1/\mu_3$ where I_1 and I_3 are the smallest and largest eigenvalues.

Figures 6 and 7 display the distribution of μ_1/μ_3 for the hydrodynamical and MHD simulations and for two thresholds 50 (upper panels) and 200 cm^{-3} (lower panels for Fig. 6 and middle panel for Fig. 7). Clearly, the aspect ratios in the MHD simulations are smaller by a factor of $\simeq 1.5$ -2 than the aspect ratios in the hydrodynamical simulations. The

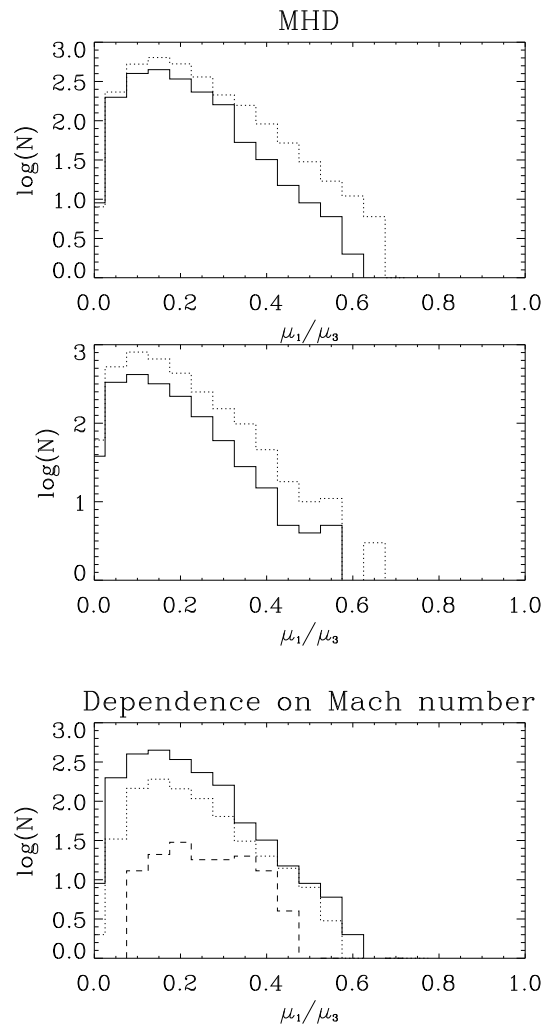


Fig. 7. Distribution of aspect ratio, μ_3/μ_1 of the clumps in the MHD simulations. Bottom panel shows the distribution for the threshold $n = 50 \text{ cm}^{-3}$ and for 3 Mach numbers (solid line: $\mathcal{M} = 10$, dashed line: $\mathcal{M} = 3$, dotted line: $\mathcal{M} = 1$). Middle and top panels show the distribution at two different thresholds (middle: 50 cm^{-3} , bottom: 200 cm^{-3}) for the fiducial simulation (magnetized, $\mathcal{M} = 10$: solid line) at time 1.81 Myr and the high resolution simulation at time 2.26 Myr (dotted line).

threshold has only a modest influence on the resulting distribution.

Bottom panel of Fig. 7 shows that the Mach number, has only a modest influence on this result. There are only little differences between $\mathcal{M} = 10$ and 3 runs (solid and dotted lines respectively). There are more differences in the $\mathcal{M} = 1$ run but this could be due to the lack of statistics. The peak is may be shifted toward slightly higher values but stays below 0.2-0.3.

It is worth stressing that in all cases, most of the clumps have an aspect ratio smaller than 0.3 and a good fraction of them have an aspect ratio smaller than 0.2 and even 0.1. These latter can be called filaments.

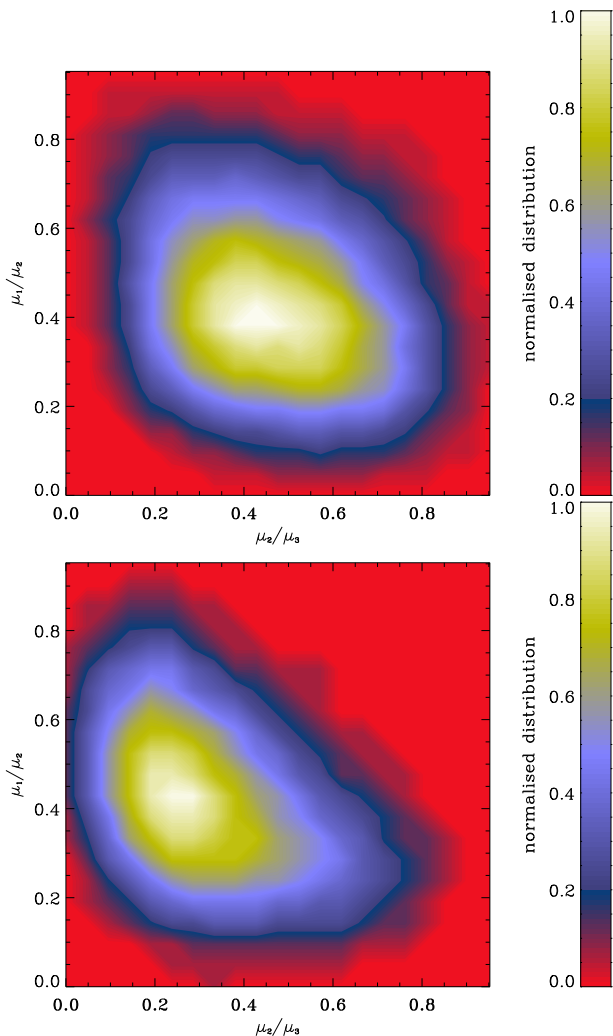


Fig. 8. Normalised bidimensional histogram displaying μ_1/μ_2 as a function of μ_2/μ_3 . Top panel: hydrodynamical simulation at time 3.37 Myrs. Bottom panel: MHD simulation at time 1.81 Myrs.

4.2.2. Triaxial clumps

The aspect ratio of the largest over smallest eigenvalues gives only a partial description of the clump geometry. It is necessary, to get a more complete description, to investigate the distribution of the two ratio μ_1/μ_2 and μ_2/μ_3 . Figure 8 displays the normalised bidimensional histograms for the hydrodynamical and MHD simulations using the density threshold of 200 cm^{-3} . The two distributions present significant differences. The clumps from the hydrodynamical simulation tend to cover more uniformly the μ_1/μ_2 - μ_2/μ_3 plane. In particular, most of the points are located in a region with $\mu_1/\mu_2 \simeq 0.2 - 0.6$ and $\mu_2/\mu_3 \simeq 0.3 - 0.8$. Such clumps can be described as ribbons or/and sheets. More quantitatively, we find that the fraction of clumps having μ_2/μ_3 between 0.2 and 0.8 and μ_1/μ_2 between 0.3 and 0.7 is 62% amongst which about half have their μ_2/μ_3 lower than 0.5. The number of clumps with μ_2/μ_3 smaller than 0.3 and μ_1/μ_2 larger than 0.4 is only about 11%. In the MHD simulation, the values $\mu_1/\mu_2 \simeq 0.5$ and $\mu_2/\mu_3 \simeq 0.25$ are more typical. Such objects can be described as ribbons and/or filaments. The most important difference are the ab-

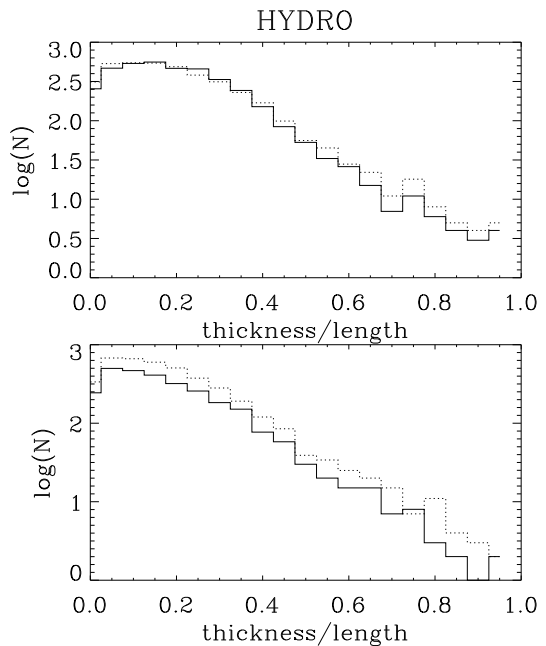


Fig. 9. Same as Fig. 6 for the distribution of the aspect ratio, R/L of the clumps (threshold 50 cm^{-3} : upper panel and 200 cm^{-3} : lower panel) in the hydrodynamical simulation at time $t = 1.52 \text{ Myr}$ (dotted lines) and $t = 3.37 \text{ Myr}$ (solid lines).

sence of spheroidal ($\mu_1 \simeq \mu_2 \simeq \mu_3$) clumps and the scarcity of sheet like clumps ($\mu_1 \ll \mu_2 \simeq \mu_3$) in the MHD simulations. More quantitatively, the fraction of clumps having μ_2/μ_3 between 0.2 and 0.8 and μ_1/μ_2 between 0.3 and 0.7 is 52% amongst which about 75% have their μ_2/μ_3 lower than 0.5. The fraction of sheet like or spheroidal like objects ($\mu_2/\mu_3 > 0.5$) is therefore two times smaller than in the hydrodynamical simulation. The number of filamentary clumps with μ_2/μ_3 smaller than 0.3 and μ_1/μ_2 larger than 0.4 is about 30% which is three times more than in the hydrodynamical simulation.

Since sheet-like objects are produced by shocks, this clearly suggests that while in the hydrodynamical simulations, shocks are important and numerous, they play a less important role in the MHD simulations. This is somehow expected because the magnetic field certainly reduces their ability to compress the gas.

4.2.3. Aspect ratio from skeleton

In order to ascertain the trends inferred for the clump aspect ratio, we have also calculated it using the skeleton approach and the definitions given in Sect. 2.2.1. The results for the two snapshots of the hydrodynamical and MHD simulations are presented in Figs. 9 and 10. As can be seen, the trends are very similar to what has been inferred from the inertia matrix and the distribution are generally quite comparable. In particular, the clumps tend to be more elongated in the MHD case than in the hydrodynamical case. One difference however is the presence of a tail of few weakly elongated clumps (aspect ratio 0.5-1) that is not apparent in the inertia matrix approach. This is likely due to the difference in the definition between the two methods.

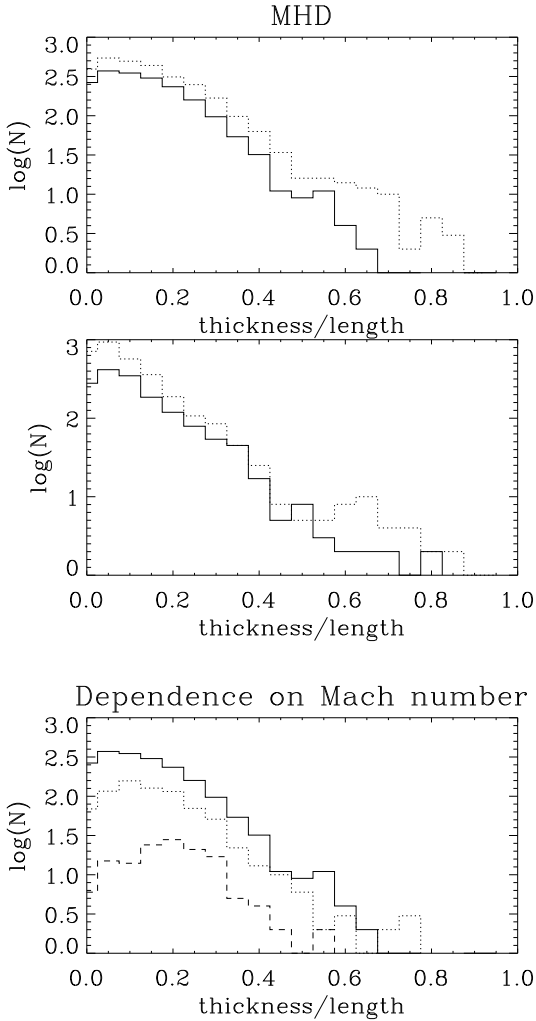


Fig. 10. Same as Fig. 7 for the distribution of the aspect ratio, R/L of the clumps. Bottom panel shows the distribution for the threshold $n = 50 \text{ cm}^{-3}$ and for 3 Mach numbers (solid line: $\mathcal{M} = 10$, dashed line: $\mathcal{M} = 3$, dotted line: $\mathcal{M} = 1$). Middle and top panels show the distribution at two different thresholds (middle: 50 cm^{-3} , bottom: 200 cm^{-3}) for the fiducial simulation (magnetized, $\mathcal{M} = 10$: solid line) at time 1.81 Myr and the high resolution simulation at time 2.26 Myr (dotted line).

The nice similarity of the distributions obtained with two completely different methods, suggests however that the two methods are indeed reliable.

4.3. Length and thickness

We now turn to the study of the clump characteristic scales. The length is defined as the sum over all $G_i^j \mathcal{G}_i^j$ within the clumps. This gives the sum of the length of all the branches which belong to the clumps and is therefore longer than the largest distance between two points in the clump. The thickness is defined as explained in Sect. 2.2.1, that is to say as the mean distance between the clump cells and the clump local direction (defined by the \mathbf{u}_i^j).

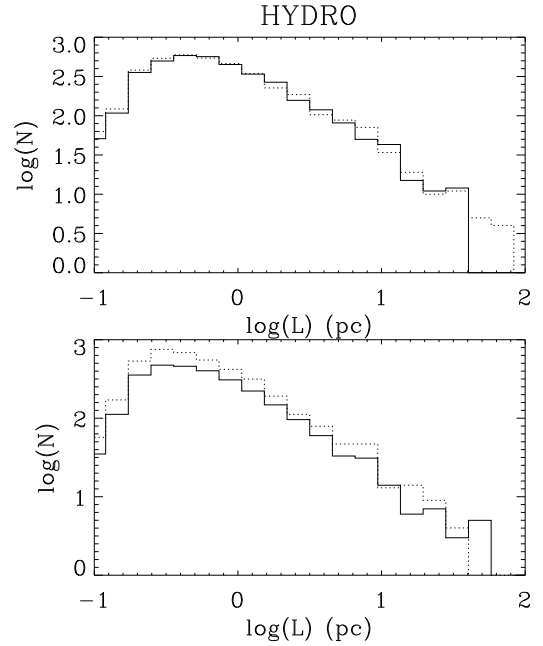


Fig. 11. Same as Fig. 6 for the distribution of the length of the clumps.

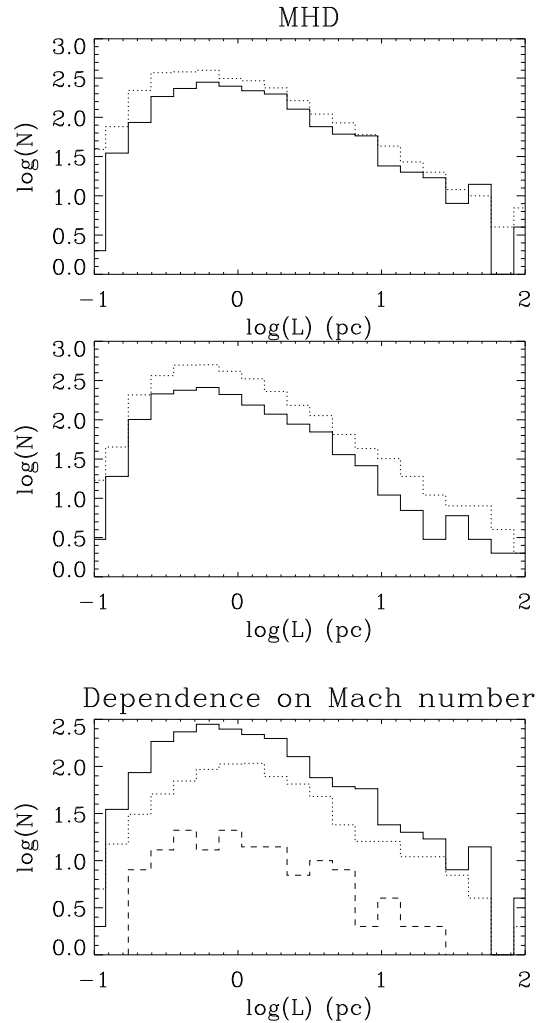


Fig. 12. Same as Fig. 7 for the distribution of the length of the clumps.

4.3.1. Clump length

Figures 11 and 12 show the length distribution for the hydrodynamical and MHD simulations respectively. The distributions are similar. They peak at about $L \simeq 0.5$ pc and decrease with size for smaller value. This is very similar to the behaviour of the clump mass spectra (e.g. Hennebelle & Audit 2007, Audit & Hennebelle 2010) and is a clear consequence of the numerical diffusion induced by the finite size of the mesh. The comparison between the fiducial simulation (top panel of Fig. 12) and the high resolution run shows that these peaks tend to shift toward the smaller size in spite of the extraction being performed at the same physical resolution as explained previously. At larger length, L , the distribution is close to a powerlaw. This is more obvious for the $\mathcal{M} = 10$ simulations than for the $\mathcal{M} = 3$ and 1 cases (bottom panel of Fig. 12) probably because there are less clumps in these simulations and the statistics are poorer. Typically we get $\mathcal{N} = dN/d\log L \propto L^{-1}$ for the threshold 200 cm^{-3} . The exponent is slightly shallower for the threshold 50 cm^{-3} . Apart from the fact that turbulence generally tends to generate powerlaws, it is worth to understand better the origin of this exponent.

First of all, it is worth recalling that the mass spectra of clumps is found to be $dN/d\log M \propto M^{-\alpha_N+1}$ with $\alpha_N \simeq 1.8$ by various authors (Hennebelle & Audit 2007, Heitsch et al. 2008, Dib et al. 2008, Audit & Hennebelle 2010, Inoue & Inutsuka 2012). This exponent is consistent with the value inferred by Hennebelle & Chabrier (2008) for turbulent clumps. Anticipating on what will be shown in the next section, the thickness of the clumps, r_c , stays roughly constant, i.e. is peaking toward a nearly constant value with a narrow distribution. But the mass of clumps is proportional to $L \times r_c^2 \rho$, thus since r_c is found to be roughly constant and that the mean density in most of the clumps is of the order of the density threshold, one finds that the mass of the clumps is proportional to its length $M \propto L$ (we recall that L is the integrated length through all branches). Consequently, it is not surprising to find that $dN/d\log L \propto L^{-1}$ which is close enough to the clump mass spectrum.

4.3.2. Clump thickness

Figures 11 and 12 show the thickness distribution for the Hydrodynamical and MHD simulations respectively. The distributions of the hydrodynamical and MHD simulations at Mach 10 show very similar behaviours. They peak at about $\simeq 0.1$ pc for both thresholds (with a small shift toward higher values for the lowest threshold 50 cm^{-3}). This is similar to the behaviour displayed by the length distribution which also present a peak, though shifted toward larger values. The high resolution simulation (middle and top panels of Fig. 12) show again a systematic trend toward smaller values. This is again consistent with the peak being due to the numerical diffusion.

Unlike for the length distribution however, there is no powerlaw tail, instead the whole distribution is a narrow peak (full width at half maximum of about 0.4). Thus we conclude that the thickness of the clumps (that also represent the thickness of filaments when only the very elongated ones are selected) is largely due to the finite resolution of the simulations. This in turns means that in order to describe physically the interstellar filaments down to their

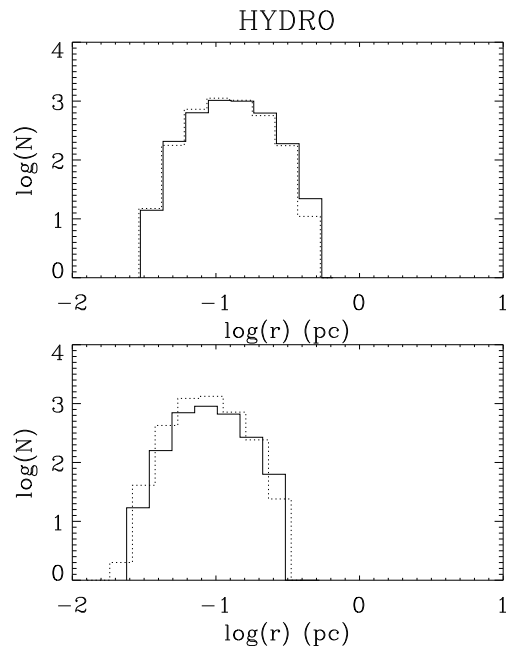


Fig. 13. Same as Fig. 6 for the distribution of the thickness of the clumps.

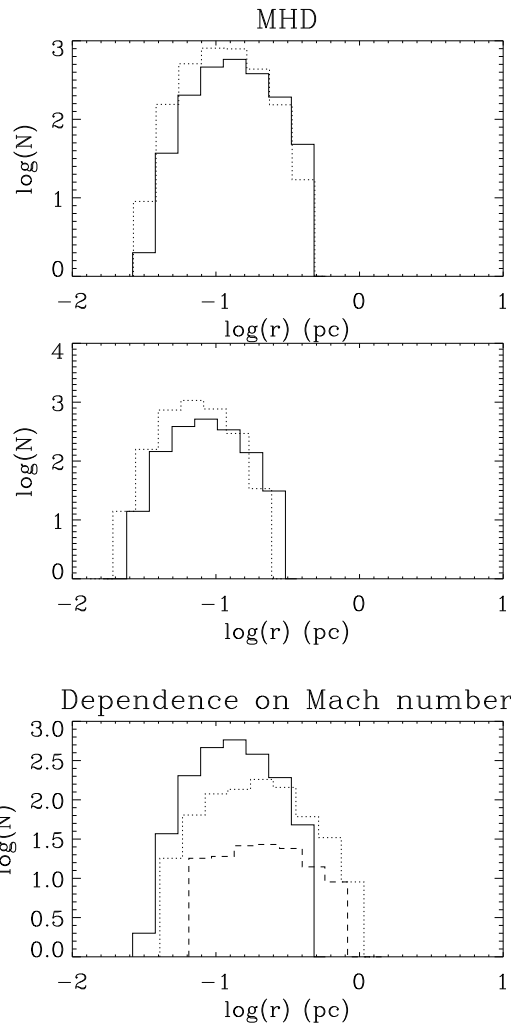


Fig. 14. Same as Fig. 7 for the distribution of the thickness of the clumps.

thickness, realistic dissipative processes should be consistently included (see the discussion section). It is worth to remind that the numerical algorithm that is used in this work is very similar to most methods implemented in other codes used in the study of the ISM and beyond. This conclusion is therefore not restricted to the present work only but seemingly affect the simulations performed with solvers which do not explicitly treat the dissipative processes. Note that if instead of the mean radius, the distribution of all the local radius is plotted, one finds that it typically extends to values of about 3-4 times larger though most of the points are still close to a few grid points.

The thickness of the clumps presents some dependence on the Mach number as shown in bottom panel of Fig. 12. However, changing the Mach number by a factor 10 leads to a shift of the size smaller than a factor 2. This contradicts the explanation of the interstellar filaments being entirely determined by shocks. A velocity perturbation at scale L has a typical amplitude $V = V_0(L/L_0)^{0.5}$ as suggested by Larson relations (Larson 1981, Falgarone et al. 2009, Hennebelle & Falgarone 2012). The Rankine-Hugoniot conditions then lead to a density enhancement $\rho_s/\rho \simeq (V/C_s)^2 = (V_0/C_s)^2 \times (L/L_0)$ and to a thickness $L_s/L = \rho/\rho_s = \mathcal{M}^2$. As can be seen the thickness is expected to vary with \mathcal{M}^2 a behaviour that we do not observe in these simulations instead a more shallow dependence on the Mach number is observed. It does not mean that compression is not playing any role. Indeed since these structures are denser than the surrounding medium, compression is occurring. However, the very reason of these structures being elongated does not seem to be a mere compression.

5. Links between geometry, velocity and forces

Next, we would like to understand why the clumps tend to have such low aspect ratio or in other words, why are there so many filaments in the simulations? So far we have seen that the MHD simulations tend to be more filamentary than the hydrodynamical ones and that the aspect ratio does not strongly evolve with the Mach number. There is only a weak trend for it to decrease when \mathcal{M} increases (bottom panel of Fig. 7). Both facts do not straightforwardly agree with the earlier proposition that filaments are due to the collision of two shocked sheets (e.g. Padoan et al. 2001) and suggest that the process entails other aspects than a mere compression. Indeed in this scenario, one would expect high Mach number flows to be more filamentary but also since magnetic field renders the collisions less supersonic, it is unclear why magnetized simulations would be more filamentary. On the other hand, the simple numerical experiment presented in Sect. 3 suggests that the filaments could simply be fluid particles that have been stretched by the turbulent motions. The most important difference with the shock scenario is that filaments are not born as elongated objects rather they become elongated as time proceeds.

In this section we investigate whether the mechanism by which filaments form is indeed the stretch of the fluid particles induced by turbulence. It should be kept in mind that shocks or say convergent motions must play a role at some stage because the gas within the filaments must accumulate. The question is then to try to estimate their respective influence.

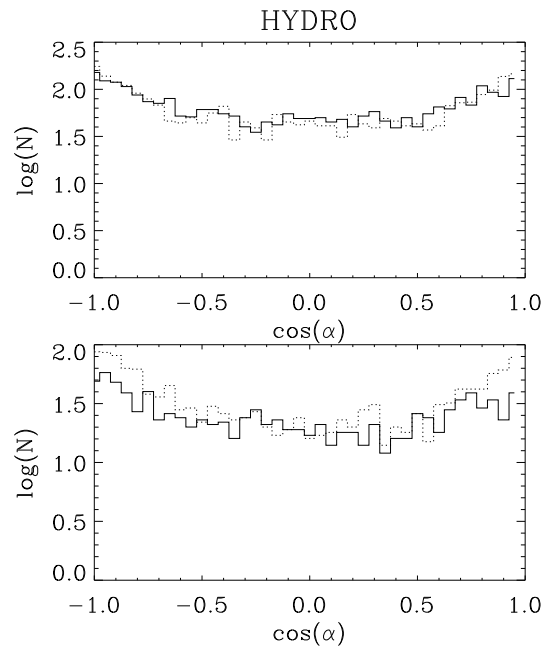


Fig. 15. Same as Fig. 6 for the distribution of $\cos \alpha$ (the angle between the main axis and the strain) in the clumps.

5.1. Alignment between strain and filament axis

To investigate whether the filaments are indeed particle fluids which have been stretched by the turbulent motions, we study the correlation between the eigenvector associated to the largest eigenvalue of the inertia matrix that we later call the axis of the filament, and the eigenvector of the largest eigenvalue of the strain tensor which gives the direction along which the clumps are stretched. More precisely, we study the distribution of $\cos \alpha$, where α is the angle between these two eigenvectors. Indeed if the two eigenvectors tend to be aligned, this will be a clear evidence that filaments are stretched by the velocity field.

Figures 15 and 16 show results for the two density thresholds. Clearly in all cases there are more clumps for which $\cos \alpha$ is close to -1 or 1 than clumps for which $\cos \alpha$ is close to 0. In other words, there is a trend for the filament axis and the strain to be aligned. This clearly shows that the primary cause of the existence of filaments, that is to say the existence of elongated clumps, is the stretching of the fluid particles induced by the turbulent motions. This does not imply that shocks may not be also forming filaments, in particular intersection between two shocked layers as it has been previously suggested. However, this cannot be the dominant mechanism because in such configurations, one would expect the filament axis and the strain to be randomly distributed.

A comparison between Figs. 15 and 16 also reveals that the trend is clearly more pronounced for MHD simulations than for hydrodynamical ones. For example, there are about 8-10 times more objects having $|\cos \alpha| = 1$ than objects with $\cos \alpha = 0$ in the MHD case. In the hydrodynamical case, this ratio is about 3 – 5. Again since the MHD simulation is more filamentary than the hydrodynamical one, this is not consistent with the dominant origin of filaments being due to shocks since magnetic field tends to reduce the effective Mach number. Finally we see that in lower Mach

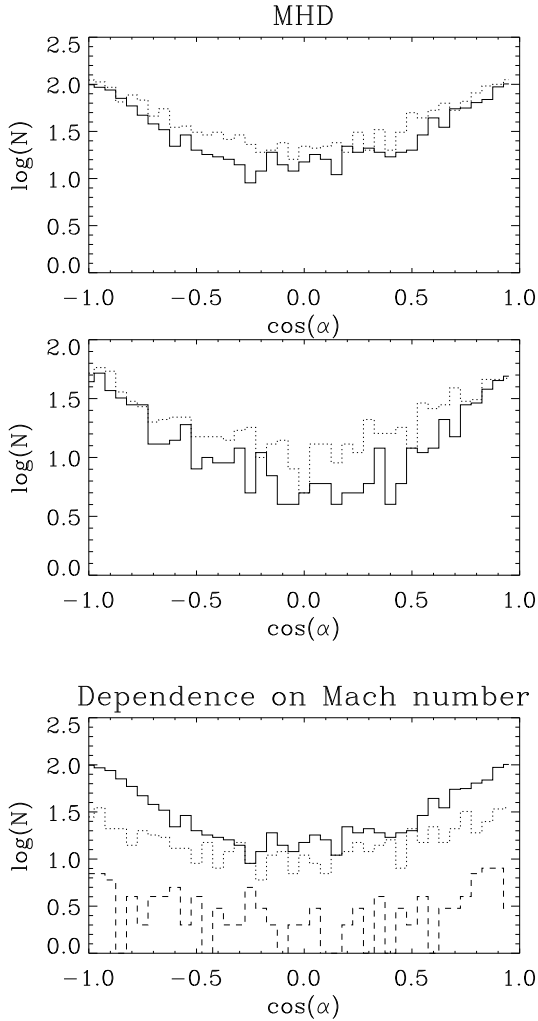


Fig. 16. Same as Fig. 7 for the distribution of $\cos \alpha$ (the angle between the main axis and the strain) in the clumps.

simulations (dotted and dashed lines of bottom panel in Fig. 16), this trends is also present but reduced.

5.2. Comparison between strain and divergence

The correlation between the strain and the filament axis suggests that strain is an important, if not the dominant reason for having filaments within the ISM. However, the clumps are regions of high densities where the gas has been accumulated. Therefore it is important to understand the respective role of the compressive motions and the straining ones. For this purpose, we study the distribution of the ratio of the divergence and the strain, r_{ds} , calculated as described in Sect. 2.2. This quantity allows us to directly estimate whether the structure is globally contracting or expanding and whether this global change of volume dominates or is dominated by the change of shape described by the strain.

Figure 17 shows results for the hydrodynamical simulation for the two thresholds (50 cm^{-3} upper panels and 200 cm^{-3} lower panels). The distribution of r_{ds} is pretty flat and extends between about -1.2 and 1.2 . It is roughly symmetrical with respect to 0 particularly for the lowest density threshold. This indicates that the contribution of compressive and solenoidal motions for the dynamics of the

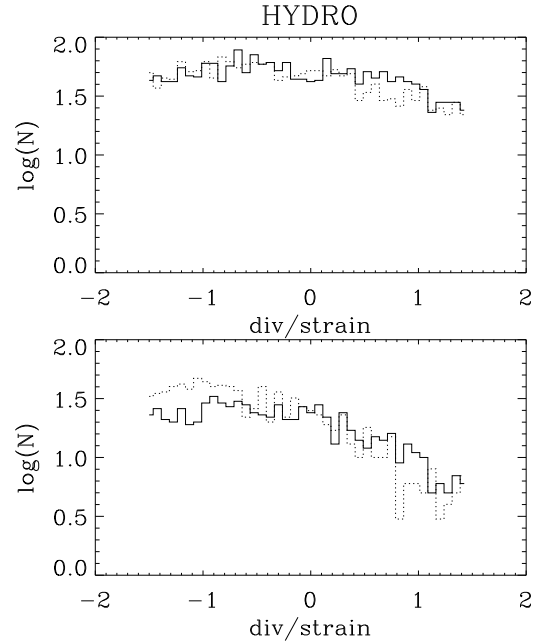


Fig. 17. Same as Fig. 6 for the distribution of the ratio of the divergence and strain in the clumps.

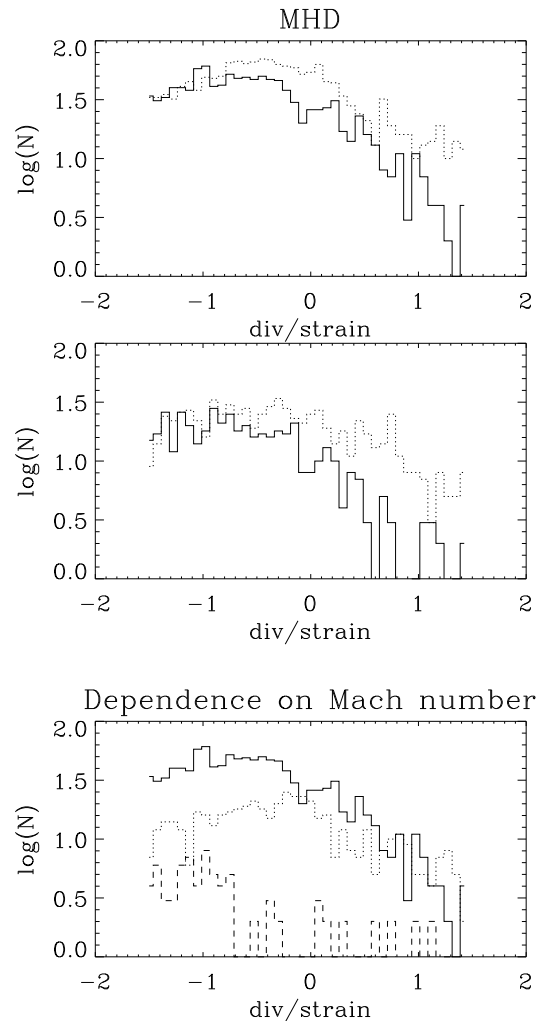


Fig. 18. Same as Fig. 7 for the distribution of the ratio of the divergence and strain in the clumps.

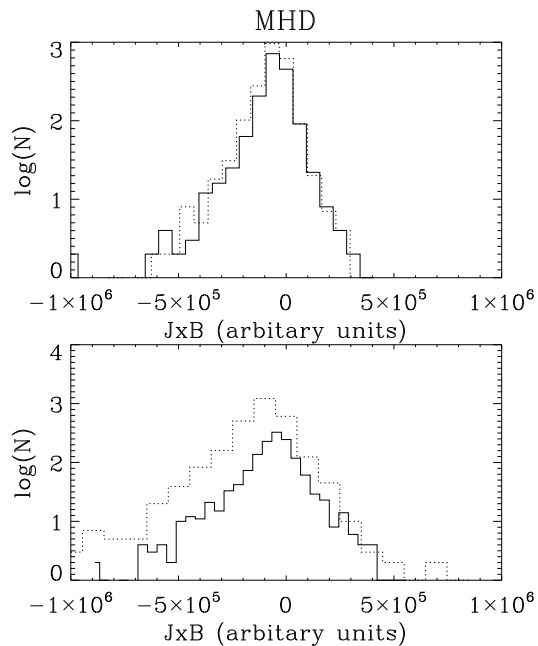


Fig. 19. Mean value of the Lorentz force radial component (see text) within the clumps. (threshold 50 cm^{-3} : upper panel and 200 cm^{-3} : lower panel) for the high resolution MHD simulation at time $t = 2.26 \text{ Myr}$ (dotted line) and the fiducial run at time 1.81 Myr (solid line).

clumps is comparable though most clumps have a mean strain larger than their divergence (but few clumps have a small r_{ds}). For our highest threshold, the number of clumps that are expanding is lower than the number of clumps that are contracting.

Figure 18 shows results for the MHD simulation. The general trends are qualitatively similar than for the hydrodynamical simulations except for the important fact that the distributions are much less symmetrical with respect to zero. There are much less expanding clumps than contracting ones. This suggests that the magnetic field tends to confine the clumps and makes their reexpansion more difficult.

Apart from this, the clear conclusion is that both compression/expansion and strain are important with the latter being generally dominant over the former.

5.3. Confinement by Lorentz force

To verify that the Lorentz force is indeed reducing the clump expansion, we have computed the mean component of the Lorentz force in the direction perpendicular to the local direction of the clumps. To accomplish this, given a cell center M , we first compute the position of M' defined by $\mathbf{GM}' = (\mathbf{u}_i^j \cdot \mathbf{GM}) \mathbf{u}_i^j$, that is to say M is projected onto the local axis in M' (u_i^j is defined as explicited in Sect. 2.2.1). The component of the force perpendicular to the local direction of the clump (\mathbf{u}_i^j) is thus simply $\mathbf{F}(\mathbf{M}) \cdot \mathbf{MM}' / |\mathbf{MM}'|$. The total contribution is thus obtained by summing over the whole structure

$$\frac{\int \mathbf{F}(\mathbf{M}) \cdot \mathbf{MM}' / |\mathbf{MM}'| dm}{\int dm}. \quad (1)$$

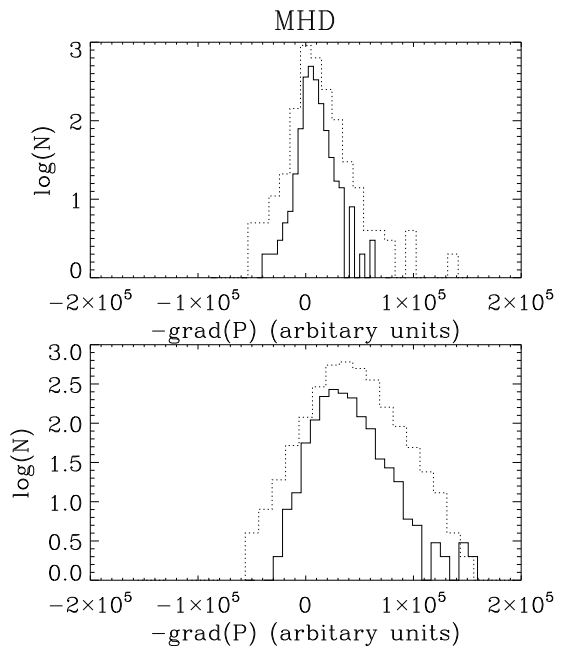


Fig. 20. Same as Fig. 19 for the mean value of the pressure force radial component (see text) within the clumps

The result is displayed in Fig. 19 for the two density thresholds. As can be seen there are structures that the Lorentz force tends globally to confine (integrated component is negative) and structures that it tends to expand. However, it is clearly skewed towards the negative values and in most cases the Lorentz force tends to confine the structure and maintain the coherence of the clumps. More quantitatively, we find that depending on the run parameters and thresholds the fraction of clumps for which the integrated component of the Lorentz force is negative, is between 55 and 65%.

For comparison, it is interesting to investigate the effect of the pressure force and the corresponding distribution is plotted in Fig. 20. As expected it is seen that the pressure force tends almost always to expand the structure. We also see from the amplitude that the Lorentz force largely dominates over the pressure force.

These results are in good agreement with the results inferred from the divergence of strain ratio, r_{ds} and also with the simple numerical experiment presented in section 3. The magnetic force tends to prevent the clump re-expansion because the magnetic field lines permeate through the clumps and connect the fluid particles together.

6. Discussion

The role played by two important processes, namely non-ideal mhd effects and gravity, has not been included or investigated in this work and require at least some discussions.

6.1. The role of dissipative processes

Although our simulations seem to roughly agree with the Herschel observations about the constancy of the filament inferred by Arzoumanian et al. (2011). It is important to keep in mind that this thickness is most likely setup in the

present simulations (and in any similar simulation) by the numerical diffusion which operates at the scale of a few computing cells (here about 0.05 pc for the fiducial run). Therefore although encouraging this resemblance must be taken with the greatest care at this stage. Moreover, our filaments are selected using a density threshold which is also different from what Arzoumanian et al. (2011) have been doing.

Nevertheless, the conclusion that the thickness of the filaments, at least in the way we define them, is setup by a dissipative process is intriguing and leads to the obvious question: which dissipative mechanism could actually produce a scale comparable to a size of 0.1 pc? The only known dissipative mechanism in the interstellar medium, which leads to comparable scales is the ion-neutral friction as investigated by Kulsrud & Pearce (1969).

Let us remind that when ion-neutral friction is taken into consideration the induction equation can be written as

$$\partial_t \mathbf{B} + \nabla \times (\mathbf{B} \times \mathbf{v}) = \nabla \times \left(\frac{1}{4\pi\gamma_{ad}\rho\rho_i} ((\nabla \times \mathbf{B}) \times \mathbf{B}) \times \mathbf{B} \right). \quad (2)$$

where γ_{ad} is the ion-neutral friction coefficient whose value is about $\gamma_{ad} \simeq 3.5 \times 10^{13} \text{ g}^{-1} \text{ s}^{-1}$ (e.g. Shu et al. 1987).

Although the right-hand side has not the standard form of a diffusion, it is a second order term which dissipates mechanical energy into heat. We can easily compute a magnetic Reynolds number associated to this equation as

$$R_{e,m} = \frac{V(l)l}{\nu}, \quad (3)$$

where $\nu = B^2/(4\pi\gamma_{ad}\rho\rho_i)$. As it is done in standard approach of turbulence, we assume that the energy flux, $\epsilon = \rho V(l)^3/l$, is constant through the scales. Thus we can write

$$R_{e,m} = \frac{\epsilon^{1/3} \rho^{-1/3} l^{4/3}}{\nu}, \quad (4)$$

Estimating ϵ at the integral scale, L_0 , we get

$$R_{e,m} = \left(\frac{\rho_0}{\rho} \right)^{1/3} \frac{V_0}{L_0^{1/3}} \frac{4\pi\gamma_{ad}\rho\rho_i}{B^2} l^{4/3}. \quad (5)$$

The smallest scale which can be reached in a turbulent cascade is typically obtained when the Reynolds number is equal to about 1. This leads for l_{diss} the dissipation length the following expression

$$l_{diss} = \left(\frac{L_0^{1/3}}{\rho_0^{1/3} V_0} \right)^{3/4} \left(\frac{B^2}{4\pi\gamma_{ad}\rho^{2/3}\rho_i} \right)^{3/4}. \quad (6)$$

The impact of non-ideal MHD processes on the density field can be clearly seen in the simulations performed by Downes & O'Sullivan (2009, 2011). These authors have run simulations of molecular clouds at the scale of 0.2 pc. The figures 1 of these two papers display the density field in the ideal MHD case and in the non-ideal MHD one. Clearly, many small scale filaments are seen in the ideal MHD simulation which evidently are very close to the numerical resolution. This is rather different from what is seen in the non-ideal MHD simulations in which only large scale structures (bigger than the cell size) are produced. Interestingly, the large scale pattern is unchanged but the small scales are completely different. These simulations demonstrate that

indeed non-ideal MHD processes have a very strong impact on the clump structure.

To estimate the dissipation length we use typical values for the diffuse interstellar medium. The values of V_0 , $\rho_0 = m_p n_0$ and L_0 are linked through the Larson relations (Larson 1981). We will choose as fiducial values $V_0 = 2.5 \text{ km s}^{-1}$, $\rho_0 = 100 \text{ cm}^{-3}$ and $L_0 = 10 \text{ pc}$. Typical magnetic fields are about $5 \mu\text{G}$ in the diffuse gas and $10\text{-}20 \mu\text{G}$ in the molecular gas for densities of a few 10^3 cm^{-3} . The ionization is also important and vary significantly.

In the molecular gas the ionization is of the order of $10^{-6} - 10^{-7}$ (Le Petit et al. 2006, Bergin & Tafalla 2007) and the ion density ρ_i can be approximated as $C\sqrt{\rho}$ where $C = 3 \times 10^{-16} \text{ cm}^{-3/2} \text{ g}^{1/2}$. Using this expression, a density of 10^3 cm^{-3} and a magnetic field of $20 \mu\text{G}$, we get $l_{diss} \simeq 0.2 \text{ pc}$ which is entirely reasonable. Note that assuming that the magnetic field increases as $\sqrt{\rho}$ (e.g. Crutcher 1999), we find that the density dependence is extremely shallow seemingly suggesting that this scale could indeed be representative of a broad range of conditions. These numbers as well as the analysis is similar to the results presented in McKee et al. (2010).

In the diffuse gas, which has a density of only a few 100 cm^{-3} , the ionization is about $10^{-4} - 10^{-5}$ (e.g. Wolfire et al. 2003) which leads for a density of 200 cm^{-3} and a magnetization of $5 \mu\text{G}$ to $l_{diss} \simeq 3 \times 10^{-3} - 2 \times 10^{-2} \text{ pc}$, that is to say much smaller values.

It is important to stress that these numbers remain indicative at this stage and should not be directly interpreted as the size of the structures which can certainly be different by a factor of a few. Nevertheless a clear consequence of these estimates is that the filaments should be much thinner in the weakly shielded gas ($A_v < 1$), in particular in the HI and at the periphery of molecular clouds.

6.2. Influence of gravity

Gravity can also play an important role in the formation of massive filaments. Indeed gravity is well known to amplify initial anisotropies (Lin et al. 1965) and has been found in various studies to play an important role in triggering the formation of self-gravitating filaments (Hartmann & Burkert 2007, Peretto et al. 2007). Indeed in these studies gravity acts to amplify the initial elongation of a clump which could have been induced by turbulence.

It is therefore likely that gravity can play a significant role in the formation of the most massive filaments and may be even for setting the width of the marginally self-gravitating ones as recently advocated by Fischera & Martin (2012).

The nature of this elongation is quite different from what has been studied here. It is a selective contraction along two directions rather than a stretching along one direction. We stress however that gravity is self-consistently included in the collision flow calculations presented in the appendix B and that as discussed in the appendix the results are very similar to what has been found for the more diffuse ISM studied in the paper. Thus it seems that except probably for very dense filaments (e.g. integral-shaped Orion or DR21 filaments), gravity may not modify the picture very significantly.

7. Conclusion

We have performed a series of numerical simulations to study the formation of clumps in the turbulent ISM paying particular attention to the reason that causes the elongation. We have run both hydrodynamical and MHD simulations and have varied the Mach number. To verify the robustness of our results, we have used two different setup namely decaying turbulence and colliding flows. To quantify the structure properties, we first extract the clumps using a simple clipping algorithm. We then compute and diagonalize the inertia matrix and the strain tensor. We also develop a skeleton-like approach which allows to infer the mean thickness and to compute whether forces tend to expand or confine the structures. We find that in all simulations most of the clumps are significantly elongated and the main axis of the structure tends to be aligned with the strain particularly in MHD simulations. The proportion of filamentary objects is higher in the MHD simulations that in the hydrodynamical ones in which a significant fraction of the clumps are sheets rather than filaments. While the pressure force tends as expected to expand the clumps, the Lorentz force tends on average to confine them allowing the filaments to persist longer. In all simulations, irrespectively of the magnetic intensity and Mach number, we find that the thickness of the clumps, that is to say the mean thickness of all the clump branches, is always close to a few computing cells seemingly suggesting that in the ISM dissipative processes are responsible of setting its value. Performing simple orders of magnitude, we find that the ion-neutral friction in regions of sufficient extinction, leads to values that are close to what has been recently inferred from Herschel observations (Arzoumanian et al. 2011). In unshielded regions like HI or in the outskirts of molecular clouds where the ionization is larger, this would imply that the filament thickness should be at least ten times smaller.

acknowledgments I thank the anonymous referee for insightful comments. I thank Pierre Lesaffre, Philippe André and Doris Arzoumanian for many related and inspiring discussions. This work was granted access to HPC resources of CINES under the allocation x2009042036 made by GENCI (Grand Equipement National de Calcul Intensif). PH acknowledge the financial support of the Agence National pour la Recherche through the COSMIS project. This research has received funding from the European Research Council under the European Community's Seventh Framework Programme (FP7/2007-2013 Grant Agreement no. 306483).

Appendix A: Results of decaying turbulence with a magnetic field tilted with respect to the mesh

As we found in this paper that in magnetized flows, the clumps are more filamentary, it is important to check that no obvious numerical artefact is producing this effect. We have thus repeated one of the runs (decaying turbulence with $5\mu\text{G}$ and one level of AMR) with a magnetic field initially tilted to 45° with respect to the mesh. Figures A.1 and A.2 show respectively the bidimensional distribution μ_1/μ_2 vs μ_2/μ_3 and the histogram of $\cos(\alpha)$, the cosine of the angle between the filament axis and the strain. As can

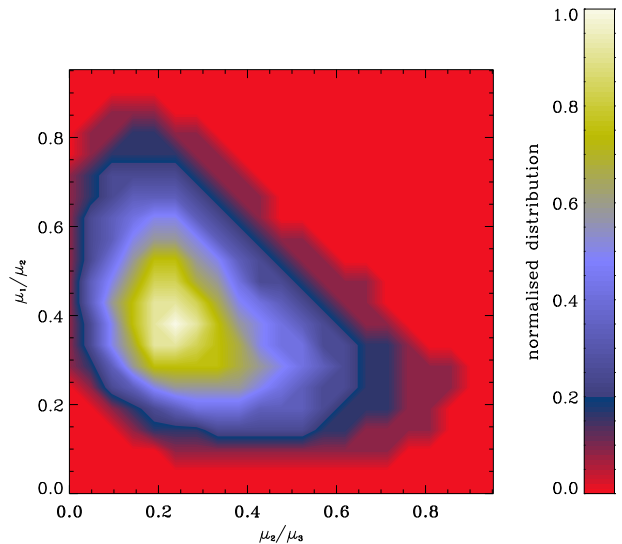


Fig. A.1. Normalised bidimensional histogram displaying μ_1/μ_2 as a function of μ_2/μ_3 for the decaying turbulence simulation with inclined magnetic field at time 1.32 Myr.

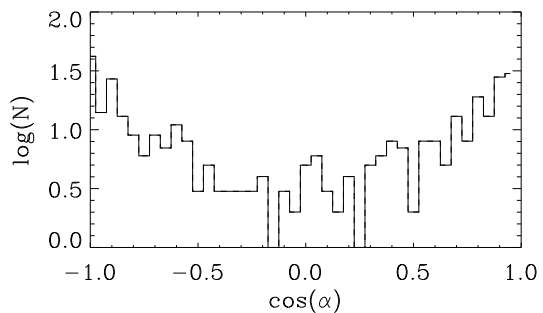


Fig. A.2. Distribution of $\cos \alpha$ (the angle between the main axis and the strain) in the clumps for the decaying turbulence simulation with inclined magnetic field at time 1.32 Myr.

be seen they are very similar to the corresponding results shown for the untilted case.

Appendix B: Results of colliding flow simulations

Here we present the results obtained for the colliding flow simulations. These simulations are described in Sect. 2.3.2. The purpose of this appendix is to demonstrate that the results obtained in the paper are not a consequence of a particular choice of initial and boundary conditions. We use timesteps which represent a comparable evolution. For the four runs, significant masses of gas (typically $10^4 M_\odot$ of gas denser than 100 cm^{-3}) have been accumulated and at several places, collapse has proceed or is still proceeding. We restrict our attention to the most important quantities that have been studied namely the clump aspect ratio computed using the inertia matrix and the skeleton-like approach, the length and thickness of the clumps, the cosine of the angle between the clump axis and the strain and the divergence over strain ratio. In the six plots the solid line represents the high resolution intermediate magnetization run, the dotted line is the standard resolution intermediate magnetization one, the dashed line represents the highly

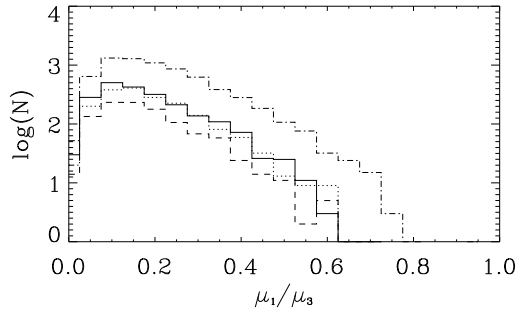


Fig. B.1. Distribution of aspect ratio, μ_3/μ_1 of the clumps (threshold 500 cm^{-3}). Solid line: high resolution intermediate magnetization run at time 12.94 Myr. Dotted line: standard resolution intermediate magnetization run at time 16.82 Myr. Dashed line: highly magnetised run at time 18 Myr. Dot-dashed line: hydrodynamical run at time 15.1 Myr.

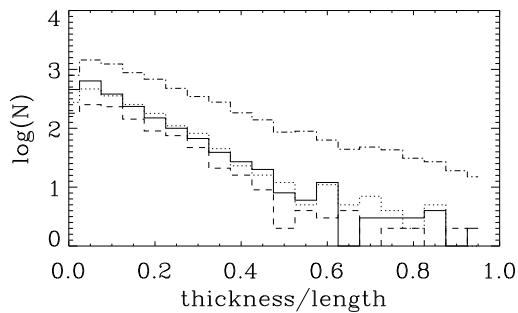


Fig. B.2. Same as Fig. B.1 for the distribution of aspect ratio, R/L of the clumps (threshold 500 cm^{-3}).

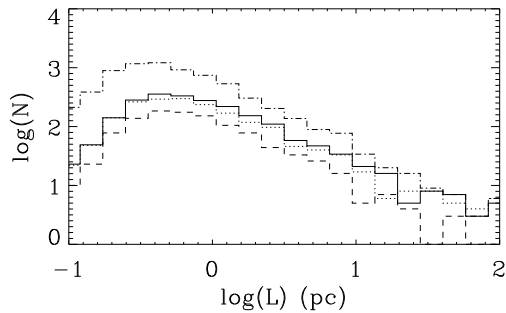


Fig. B.3. Same as Fig. B.1 for the distribution of the length of the clumps.

magnetised run while the dot-dashed displays the hydrodynamical simulation.

Figures B.1 and B.2 show very similar trends with Figs. 6, 7, 9 and 10. In particular, in the hydrodynamical simulation the clumps have larger aspect ratios than in the MHD simulations.

The length and the thickness of the clumps are very similar to what has been inferred in the decaying simulations. The peaks are also located at the same position of about 0.5 pc for the length and 0.1 pc for the thickness.

In Fig. B.5 the trends of the filament axis and the strain to be preferentially aligned is also clear. As for the decay-

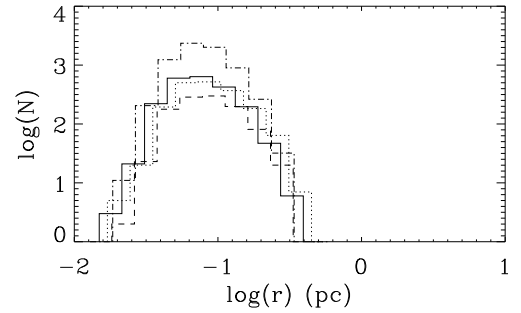


Fig. B.4. Same as Fig. B.1 for the distribution of the thickness of the clumps.

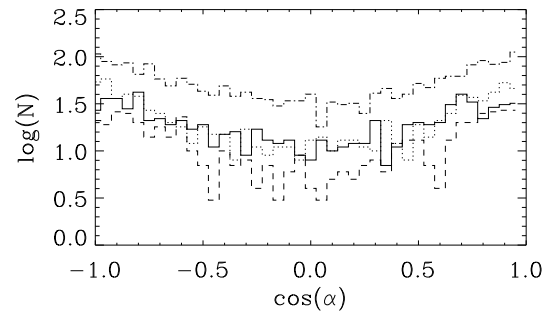


Fig. B.5. Same as Fig. B.1 for the distribution of $\cos \alpha$ (the angle between the main axis and the strain) in the clumps.

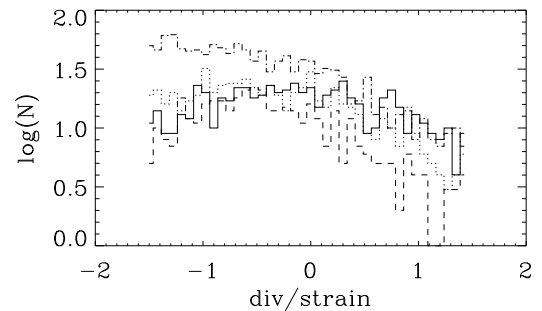


Fig. B.6. Same as Fig. B.1 for the distribution of the ratio of the divergence and strain in the clumps.

ing turbulence simulations, it is more pronounced for the magnetised runs than for the hydrodynamical runs.

Figure B.6 is also very similar to the trends inferred in Figs. 17 and 18 and discussed previously.

References

- André, P., Men'shchikov, A., Bontemps, S. et al. A&A, 2010, 518, L102
 Arzoumanian, D., André, Ph, Didelon, P. et al., 2011, A&A, 529, L6
 de Avillez M., Breitschwerdt D., 2005, A&A 436, 585
 Audit E., Hennebelle P., 2005, A&A 433, 1
 Bally, J., Lanber, W., Stark, A., Wilson, R., 1987, ApJ, 312, L45
 Banerjee, R., Vázquez-Semadeni, E., Hennebelle, P., Klessen, R., 2009, MNRAS, 398, 1082
 Bergin, E., Tafalla, M., 2007, ARA&A, 35, 179
 Crutcher, R., 1999, ApJ, 520, 706
 Dib, S., Brandenburg, A., Kim, J., Gopinathan, M., André, P., 2008, ApJ, 678, L105

- Downes, T., O'Sullivan, S., ApJ, 701, 1258, 2009
Downes, T., O'Sullivan, S., ApJ, 730, 12, 2011
Falgarone, E., Pety, J., Hily-Blant, P., 2009, A&A, 507, 355
Federrath, C., Klessen, R., 2013, ApJ, 763, 51
Fischera, J., Martin, P., 2012, A&A, 542, 77
Frank, A., Jones, T., Ryu, D., Gaalaas, J., 1996, ApJ, 460, 777
Fromang, S., Hennebelle, P., Teyssier, R., 2006, A&A, 457, 371
Hartmann, L., Burkert, A., 2007, ApJ, 654, 988
Heitsch F., Burkert A., Hartmann L., Slyz A., Devriendt J., 2005, ApJ, 633, 113
Heitsch F., Hartmann L., Slyz A., Devriendt J., Burkert A., 2008, ApJ, 674, 316
Hennebelle, P., Audit, E., 2007, A&A, 465, 431
Hennebelle, P., Chabrier, G., 2008, ApJ, 684, 395
Hennebelle, P., Banerjee, R., Vázquez-Semadeni, E., Klessen, R., Audit, E., 2008, A&A, 486, L43
Hennebelle, P., Falgarone, E., A&ARv, 20, 55
Inoue, T., Yamazaki, R., Inutsuka, S.-i., 2009, ApJ, 695, 825
Inoue, T., Inutsuka, S.-I., 2012, ApJ, 759, 35
Joung, R., Mac Low, M.-M., 2006, ApJ, 653, 1266
Kulsrud, R., Pearce, W., 1969, ApJ, 156, 445
Larson, R., 1981, MNRAS, 194, 809
Le Petit, F., Nehmé, C., Le Bourlot, J., Roueff, E., 2006, ApJS, 164, 506
Low, F., Young, E., Beintema, D. et al. 1984, ApJ, 278, L19
McKee, C., Li, P.-S., Klein, R., 2010, ApJ, 720, 1612
Miville-Deschênes, M.-A., Martin, P., Abergel, A., 2010, A&A, 518, L104
Miyoshi, T., Kusano, K., 2005, JCoPh, 208, 315
Nagai, T., Inutsuka, S.-I., Miyama, S., 1998, ApJ, 506, 306
Nakamura, F., Li, Z.-Y., 2008, ApJ, 687, 354
Padoan, P., Juvella, M., Goodman, A., Nordlund, A., 2001, ApJ, 553, 227
Padoan, P., Nordlund, A., Kritsuk, A., Norman, M., Li, P.-S., 2007, ApJ, 661, 972
Peretto, N., Hennebelle, P., André, P., A&A, 2007, 464, 983
Price, D., Bate, M., 2008, MNRAS, 385, 1820
Ryu, D., Jones, T., Frank, A., 2000, ApJ, 545, 475
Seifreid, D., Schmidt, W., Niemeyer, J. 2011, A&A, 526, 14
Sousbie, T. Colombi, S., Pichon, C., 2009, MNRAS, 393, 457
Shu, F. H., Adams, F. C., Lizano, S. 1987, ARA&A 25, 23
Teyssier, R., 2002, A&A, 385, 337
Ungerechts, H., Thaddeus, P., 1987, ApJS, 63, 645
Vázquez-Semadeni, E., Banerjee, R., Gómez, G., Hennebelle, P., Duffin, D., Klessen, R., 2011, MNRAS, 414, 2511
Ward-Thompson, D., Kirk, J., André, P., 2010, A&A, 518, L92
Wolfire M.G., Hollenbach D., McKee C.F., 1995, ApJ 443, 152
Wolfire M.G., Hollenbach D., McKee C.F., 2003, ApJ 587, 278